




Proceedings Article

A deep equilibrium technique for 3D MPI reconstruction

Alper Güngör ^{a,b,*}. Emine Ulku Saritas ^{a,c}. Tolga Çukur ^{a,c}

^aDepartment of Electrical and Electronics Engineering, Bilkent University, Ankara, Turkey

^bAselsan Research Center, Ankara, Turkey

^cNational Magnetic Resonance Research Center (UMRAM), Bilkent University, Ankara, Turkey

*Corresponding author, email: alperg@ee.bilkent.edu.tr

© 2024 Güngör *et al.*; licensee Infinite Science Publishing GmbH

This is an Open Access article distributed under the terms of the Creative Commons Attribution License (<http://creativecommons.org/licenses/by/4.0>), which permits unrestricted use, distribution, and reproduction in any medium, provided the original work is properly cited.

Abstract

Image reconstruction in MPI involves estimation of the particle concentration given acquired data and system matrix (SM). As this is an ill-posed inverse problem, image quality depends heavily on the prior information used to improve problem conditioning. Recent learning-based priors show great promise for MPI reconstruction, but priors purely driven by image samples in training datasets can show limited reliability and generalization. Here, we propose 3DEQ-MPI, a new deep equilibrium technique for 3D MPI reconstruction. 3DEQ-MPI is based on an infinitely-unrolled network architecture that synergistically leverages a data-driven prior to learn attributes of MPI images and a physics-driven prior to enforce fidelity to acquired data based on the SM. 3DEQ-MPI is trained on a simulated dataset, and unlike common deep equilibrium models, it utilizes a Jacobian-free backpropagation algorithm for fast and stable convergence. Demonstrations on simulated data and experimental OpenMPI data clearly show the superior performance of 3DEQ-MPI against competing methods.

1. Introduction

MPI offers exceptional contrast and sensitivity in imaging of magnetic nanoparticle (MNP) distributions. Given acquired data and the system matrix (SM), image reconstruction requires solution of an ill-posed inverse problem that benefits from regularization via image priors [1]. Traditional reconstruction methods typically use hand-crafted priors, such as ℓ_2 -norm or ℓ_1 -norm, that may diverge from the underlying image distribution [2, 3]. Recent studies have instead proposed powerful learning-based priors to capture latent attributes of the image distribution from a training set [4–9]. However, purely data-driven priors that neglect physical constraints regarding the measurements can show poor reliability under inherent distributional variations between the training and test sets, even on the same imaging system [6, 7]. Thus, deep-learning (DL) approaches that respect physical constraints are direly needed for performant reconstruction in MPI.

Several recent MPI studies have proposed promising DL methods that integrate the SM into the reconstruction model. Deep-image-prior (DIP) methods synthesize MPI images natively regularized by convolutional kernels, whose weights are determined at test time via a compute-intensive optimization to ensure consistency to acquired data [4, 5]. Plug-and-play MPI (PP-MPI) embeds an image denoiser pre-trained on simulated MPI data into an iterative optimization for alternating between denoising and data-consistency projections [9]. Unrolled methods perform end-to-end training of a cascaded architecture interleaving convolution and data-consistency blocks [10]. DL approaches commonly use complex network architectures with millions of parameters, resulting in heavy computational burden. As such, some previous DL-based MPI methods have devised 2D models for cross-sectional processing to alleviate burden [9]. Yet, exploiting volumetric spatial context in MPI images can improve reconstructions.

Here, we introduce 3DEQ-MPI, a new DL-based method for volumetric MPI reconstruction based on a deep equilibrium technique. In a recent study, we have examined the utility of deep equilibrium models for 2D MPI reconstruction, where computational benefits were observed over previous state-of-the-art methods [10]. However, the 2D DEQ model does not leverage correlated information in the through-plane direction of MPI volumes, potentially limiting reconstruction performance. Furthermore, the 2D DEQ model uses Jacobian backpropagation, whose training time does not scale well to 3D reconstruction given the elevated model complexity. Hence, our contributions over [10] are three-fold: (1) 3DEQ-MPI leverages a 3D convolutional network architecture to better model volumetric spatial context [11]. (2) 3DEQ-MPI employs a Jacobian-free backpropagation algorithm in contrast to Jacobian backpropagation that can be susceptible to poor convergence. (3) 3DEQ-MPI provides 3D MPI reconstructions, enabling comparisons with other methods on the publicly available OpenMPI dataset. We provide demonstrations on simulated and OpenMPI [12] datasets that indicate that 3DEQ-MPI produces superior reconstructions to existing methods.

II. Theory

II.1. MPI Reconstruction

The imaging forward model for MPI is expressed as:

$$\mathbf{Ax} + \mathbf{n} = \mathbf{y}, \quad (1)$$

where $\mathbf{A} \in \mathbb{R}^{M \times N}$, $\mathbf{x} \in \mathbb{R}^N$, $\mathbf{n} \in \mathbb{R}^M$ and $\mathbf{y} \in \mathbb{R}^M$ are the SM measured via a calibration scan, image vector, noise vector and data vector, respectively; M and N are the number of frequency components and the grid-size, respectively. The inverse problem for reconstruction can then be expressed as [3, 13, 14]:

$$\arg \min_{\mathbf{x}} R(\mathbf{x}) + \lambda/2 \|\mathbf{Ax} - \mathbf{y}\|_2^2, \quad (2)$$

where $R(\cdot)$ denotes the regularization due to the image prior on \mathbf{x} , and λ controls the relative balance between regularization and consistency to the acquired data.

II.2. 3DEQ-MPI

3DEQ-MPI is a deep equilibrium technique for 3D MPI reconstruction based on a physics-driven unrolled architecture, where convolutional blocks (CNN) and data-consistency (DC) blocks are utilized within multiple iterations of an alternating direction method of multipliers (ADMM) algorithm. CNNs are implemented as a residual-dense network [10, 11] adapted for volumetric processing by replacing 2D with 3D convolution operators. A fixed-point iteration through the unrolled architecture

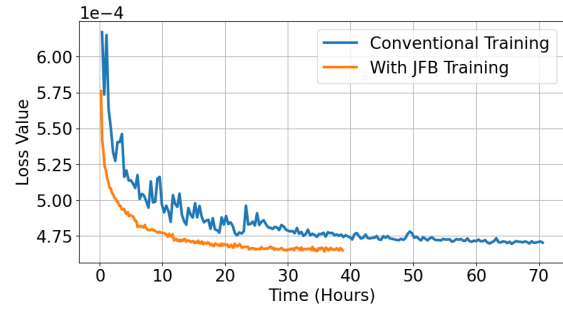


Figure 1: Training losses of 3DEQ-MPI variants with the proposed Jacobian-free backpropagation (JFB training, orange) and Jacobian backpropagation (conventional training, blue). Loss is plotted as a function of training time.

is given as $\mathbf{x}_{k+1} = h_{\theta}(\mathbf{x}_k; \mathbf{y}, \mathbf{A})$ with parameters θ . To lower memory load for storing gradients across multiple iterations, 3DEQ-MPI iterates until a convergent solution $\mathbf{x}_* = h_{\theta}(\mathbf{x}_*; \mathbf{y}, \mathbf{A})$, and learns θ based on the final iteration:

$$\arg \min_{\theta} \left\| h_{\theta}(\mathbf{x}_*; \mathbf{y}, \mathbf{A}) - \hat{\mathbf{x}}_r \right\|_1, \quad (3)$$

where $\hat{\mathbf{x}}_r$ is the ground-truth image. During training, \mathbf{y} was obtained by multiplying simulated phantom images ($\hat{\mathbf{x}}_r$) with experimental SMs (\mathbf{A}) and adding white Gaussian noise.

Common DEQ methods solve Eq. (3) by evaluating the Jacobian of the convergent solution:

$$\frac{\partial \mathbf{x}_*}{\partial \theta} = \frac{\partial h_{\theta}(\mathbf{x}_*)}{\partial \mathbf{x}_*} \frac{\partial \mathbf{x}_*}{\partial \theta} + \frac{\partial h_{\theta}(\mathbf{x}_*)}{\partial \theta}, \quad (4)$$

$$\frac{\partial \mathbf{x}_*}{\partial \theta} = \left(\mathbf{I} - \frac{\partial h_{\theta}(\mathbf{x}_*)}{\partial \mathbf{x}_*} \right)^{-1} \frac{\partial h_{\theta}(\mathbf{x}_*)}{\partial \theta}. \quad (5)$$

However, calculation of the inverse in Eq. (5) requires an iterative algorithm involving gradients that can show high computational burden and poor training stability. To improve computational efficiency and stability, here we adopt a Jacobian-free backpropagation (JFB) algorithm where the network is treated as a single-iteration architecture at the convergent solution to avoid the need for iterative gradient computations [15]. Fig. 1 displays the training loss curves of 3DEQ-MPI variants implemented based on JFB versus conventional Jacobian backpropagation. Due to its improved convergence rate, JFB reaches specific loss values in about 2-10 fold shorter training times than the conventional algorithm.

III. Methods

III.1. Phantom Dataset

3DEQ-MPI was trained on a simulated phantom dataset. 3D phantoms were generated by superposing N_e ellipsoids ($1 \leq N_e \leq 5$) within a $95 \times 95 \times 95$ imaging grid. Each

Table 1: Quantitative evaluations on simulated phantoms. pSNR (dB) listed as mean \pm std across the test set.

	SNR=0 dB	SNR=10 dB
ART	26.37 \pm 3.36	29.96 \pm 1.87
ADMM (ℓ_1)	21.87 \pm 1.72	31.34 \pm 4.18
ADMM (TV)	30.45 \pm 2.76	34.02 \pm 3.08
ADMM (ℓ_1 &TV)	30.56 \pm 2.93	34.58 \pm 3.27
PP-MPI 2D	29.49 \pm 1.91	33.30 \pm 2.04
PP-MPI 3D	35.72 \pm 4.79	43.18 \pm 4.72
Unrolled ADMM	34.91 \pm 1.84	41.27 \pm 2.25
3DEQ-MPI	39.21 \pm 3.85	45.95 \pm 4.43

Table 2: Run times (msec) and number of iterations while reconstructing the shape phantom in the OpenMPI dataset.

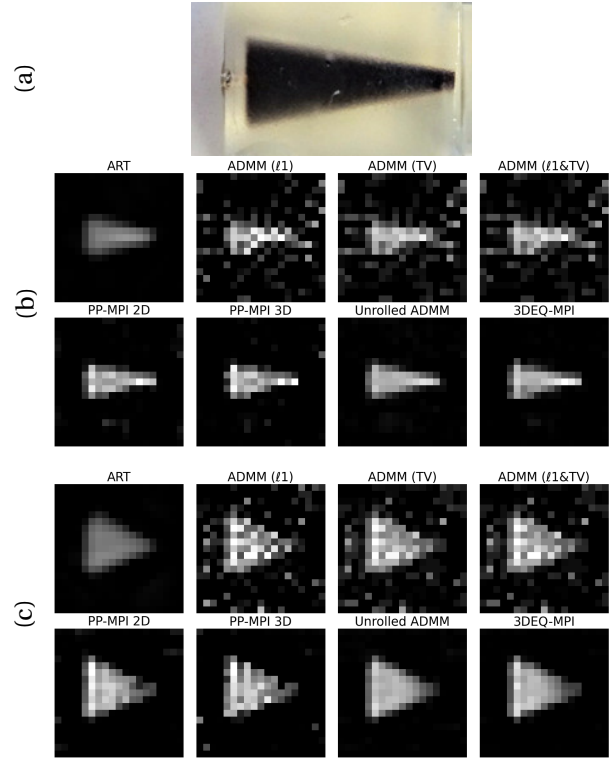
	Run time	# of iter.
ART	8138.4	10
ADMM (ℓ_1)	253.7	250
ADMM (TV)	919.6	250
ADMM (ℓ_1 &TV)	1872.3	500
PP-MPI 2D	503.0	100
PP-MPI 3D	264.5	100
Unrolled ADMM	15.3	5
3DEQ-MPI	77.0	25

ellipsoid had random radii and center-location within the grid. Each phantom was downsampled to $19 \times 19 \times 19$ to match the SM size in OpenMPI, and normalized to a maximum intensity between 0.5 and 1.5. Here, we restricted the experiments to deployment scenarios in which the maximum intensity of the imaged phantom is roughly pre-estimated. In cases where prior estimate is unavailable, reliability of reconstructions can be improved by using a training dataset of phantoms that span across a broader range of maximum intensities to cope with potential variations, or by adopting the scaling technique introduced in [16]. A total of 40000 phantoms were generated, with a non-overlapping (30000, 5000, 5000) split for (training, validation, test) sets.

III.II. Experiments

Demonstrations were performed on the simulated phantom dataset and the experimental OpenMPI dataset. In both cases, an SM from OpenMPI (SM #3) was used [12]. For each competing method, hyperparameters were optimized on the validation set. For the simulated dataset, data were generated by multiplying the SM with the simulated phantom images followed by white Gaussian noise addition [10]. Noise was added at two different levels to attain signal-to-noise-ratios (SNR) of 0 and 10 dB. The quality of the reconstructed images was measured via peak SNR (pSNR):

$$pSNR(\mathbf{x}_*, \hat{\mathbf{x}}_r) = 20 \log_{10} \left(\sqrt{N} / \|\mathbf{x}_* - \hat{\mathbf{x}}_r\| \right) \quad (6)$$

**Figure 2:** (a) Reference image depicting the shape phantom [12]. Representative experimental results in (b) x-y and (c) x-z planes of reconstructions of the shape phantom from the OpenMPI dataset.

where \mathbf{x}_* is the reconstructed image. For the experimental dataset, visual inspections were conducted instead since ground-truth phantom images are unavailable.

IV. Results

Table 1 lists the pSNR values for the competing methods (see [10] for method details) evaluated on the simulated dataset. For each competing method, hyperparameters were selected to maximize validation performance on the simulated phantom dataset, and the number of iterations were set by continuing iterations until a convergent solution is reached. Note that except for PP-MPI 2D proposed in [9], all other DL methods were 3D and were developed within the scope of this work. While TV regularization helps improve reconstructions of piece-wise constant ellipsoid shapes, traditional methods (ART and ADMM variants) perform poorly in general when compared to DL methods. Among the DL methods, 3D models (PP-MPI 3D, Unrolled ADMM, 3DEQ-MPI) perform favorably against the 2D model (PP-MPI 2D), showcasing the benefit of exploiting volumetric context. Overall, 3DEQ-MPI is the top performer with an average 10 dB pSNR improvement over competing methods. Compared against its closest competitor, 3DEQ-

MPI achieves a 3.39 dB improvement at SNR=0 dB and a 2.77 dB improvement at SNR=10 dB.

Figure 2 (a) and (b) display representative experimental results from the OpenMPI shape phantom. Among the traditional methods, ART yields spatially-smooth images with low contrast, and ADMM variants suffer from high noise amplification. Among the DL methods, PP-MPI models have residual pixel artifacts on the phantom/background, and the unrolled model has a visible level of smoothing and contrast loss. Meanwhile, when compared against the competing methods, 3DEQ-MPI effectively leverages volumetric context to recover the cone-shaped phantom with relatively low artifact/noise while avoiding over-smoothing.

Finally, Table 2 summarizes the run times and number of iterations for the competing methods that were used to reconstruct the OpenMPI shape phantom. For fair comparison among the methods, uncompressed system matrices were utilized during reconstruction [9]. Methods were implemented using the PyTorch library and executed on a server equipped with a Nvidia Tesla V100 GPU. We find that 3DEQ-MPI attains faster reconstructions than all competing methods, except for unrolled ADMM that converges in fewer iterations, and that 3DEQ-MPI is capable of real-time processing (>12 frames-per-second) of volumetric MPI data.

V. Conclusion

Here, we presented 3DEQ-MPI as a performant and efficient technique for 3D MPI reconstruction. 3DEQ-MPI employs an unrolled network architecture that cascades 3D CNN blocks for learnable regularization with DC blocks for enforcing fidelity to the physics of MPI measurements. 3DEQ-MPI iterates its reconstructions until convergence, and performs backpropagation on the convergent solution to mitigate memory burden. To further improve training speed and stability, a Jacobian-free algorithm is adopted for optimizing the parameters of 3DEQ-MPI. Demonstrations on simulated ellipsoidal phantom and experimental OpenMPI datasets clearly show the superior performance of 3DEQ-MPI against previous traditional and learning-based MPI methods.

Acknowledgments

This work was supported by the Scientific and Technological Research Council of Turkey (TUBITAK 22AG016/23AG005).

Author's statement

Conflict of interest: Authors state no conflict of interest.

References

- [1] B. Gleich and J. Weizenecker. Tomographic imaging using the nonlinear response of magnetic particles. *Nature*, 435(7046):1214–1217, 2005.
- [2] T. Knopp, J. Rahmer, T. F. Sattel, S. Biederer, J. Weizenecker, B. Gleich, J. Borgert, and T. M. Buzug. Weighted iterative reconstruction for magnetic particle imaging. *Phys Med Biol*, 55(6):1577–1589, 2010.
- [3] S. Ilbey, C. B. Top, A. Güngör, T. Çukur, E. U. Saritas, and H. E. Güven. Comparison of system-matrix-based and projection-based reconstructions for field free line magnetic particle imaging. *IJMPI*, 3(1):1703022, 2017.
- [4] S. Dittmer, T. Kluth, D. O. Bagger, and P. Maass, A deep prior approach to magnetic particle imaging, in *MLMIR*, 113–122, Springer, 2020.
- [5] T. Knopp and M. Grosser, Warmstart approach for accelerating deep image prior reconstruction in dynamic tomography, in *MIDL*, 713–725, PMLR, 2022.
- [6] B. G. Chae. Neural network image reconstruction for magnetic particle imaging. *ETRI J*, 39(6):841–850, 2017.
- [7] P. Koch, M. Maass, M. Bruhns, C. Droigk, T. J. Parbs, and A. Mertins, Neural network for reconstruction of MPI images, in *IWMPI*, 39–40, 2019.
- [8] X. Wu, B. He, P. Gao, P. Zhang, Y. Shang, L. Zhang, J. Zhong, J. Jiang, H. Hui, and J. Tian. PGNet: Projection generative network for sparse-view reconstruction of projection-based magnetic particle imaging. *Med Phys*, 50(4):2354–2371, 2023.
- [9] B. Askin, A. Güngör, D. Alptekin Soydan, E. U. Saritas, C. B. Top, and T. Çukur, PP-MPI: A deep plug-and-play prior for magnetic particle imaging reconstruction, in *MLMIR*, Springer, 105–114, 2022.
- [10] A. Güngör, B. Askin, D. A. Soydan, C. B. Top, E. U. Saritas, and T. Çukur. DEQ-MPI: A deep equilibrium reconstruction with learned consistency for magnetic particle imaging. *IEEE Trans Med Imaging*, doi:10.1109/TMI.2023.3300704, 2023.
- [11] Y. Zhang, Y. Tian, Y. Kong, B. Zhong, and Y. Fu. Residual dense network for image restoration. *IEEE Trans Pattern Anal Mach Intell*, 43(7):2480–2495, 2021.
- [12] T. Knopp, P. Szwargulski, F. Griese, and M. Gräser. OpenMPIData: An initiative for freely accessible magnetic particle imaging data. *Data Brief*, 28:104971, 2020.
- [13] A. Güngör, B. Askin, D. A. Soydan, E. U. Saritas, C. B. Top, and T. Çukur. TranSMS: Transformers for super-resolution calibration in magnetic particle imaging. *IEEE Trans Med Imaging*, 41(12):3562–3574, 2022.
- [14] S. Ilbey, C. B. Top, A. Güngör, T. Çukur, E. U. Saritas, and H. E. Güven. Fast system calibration with coded calibration scenes for magnetic particle imaging. *IEEE Trans Med Imaging*, 38(9):2070–2080, 2019.
- [15] S. W. Fung, H. Heaton, Q. Li, D. McKenzie, S. Osher, and W. Yin, Jfb: Jacobian-free backpropagation for implicit networks, in *AAAI Conf Artif Intell*, 36, 6648–6656, AAAI, 2022.
- [16] A. Güngör, B. Aşkın, D. A. Soydan, E. U. Saritas, C. B. Top, and T. Çukur. A denoiser scaling technique for plug-and-play MPI reconstruction. *IJMPI*, 9(1):2303041, 2023.